Contents list available at CBIORE journal website

International Journal of Renewable Energy Development

Journal homepage: https://ijred.cbiore.id

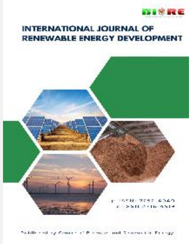

Research Article

Control synthesis of battery-supercapacitor hybrid power sources system subject to parameter variations and input saturations

Adnan Rafi Al Tahtawi[a,c], Arief Syaichu Rohman[b*], Pranoto Hidaya Rusmin[b], Arwindra Rizqiawan[b]

[a] *Doctoral Program of Electrical Engineering and Informatics, Institut Teknologi Bandung, Indonesia*

[b] *School of Electrical Engineering and Informatics, Institut Teknologi Bandung, Indonesia*

[c] *Department of Electrical Engineering, Politeknik Negeri Bandung, Indonesia*

Abstract. In practical Battery–Supercapacitor Hybrid Power Source (Batt-SC HPS) applications for Electric Vehicles (EVs), parameter variations and actuator input constraints are unavoidable due to changing operating conditions, temperature effects, and physical limitations of power converters and switching devices. These conditions may degrade control performance and potentially lead to closed-loop instability. This paper proposes a control synthesis for a Batt-SC HPS system that guarantees closed-loop stability in the presence of parameter variations and input saturations. A polytopic linear parameter-varying (LPV) model is employed to represent parameter variations in the linearized system around its equilibrium point. Based on this model, a full state-feedback controller is synthesized using simultaneous linear matrix inequalities (LMIs) as sufficient conditions for robust stability across all system vertices. The formulated LMIs incorporate a common quadratic Lyapunov function, L2-gain performance, and sector nonlinearity to explicitly handle control input saturations. Numerical validation is performed under internal resistance variation scenarios using an LMI solver. Closed-loop simulation results show that the proposed controller reduces the battery current RMSE by 70.8% and the DC bus voltage RMSE by 87.4% compared with a conventional PID controller. In comparison with a nominal LTI controller, additional RMSE reductions of 38.31% for battery current and 2.82% for DC bus voltage are achieved. Moreover, the proposed controller maintains comparable energy consumption characteristics, with total energy differences of only 0.22% and 0.11% relative to the PID and LTI controllers. These results demonstrate the potential of the proposed controller for robust stabilization of Batt-SC HPS systems in EV applications.

Keywords: Polytopic model, LMI-based state-feedback, Batt-SC HPS, parameter variations, saturations

Received: 9th Feb 2026; Revised: 27th April 2026; Accepted: 28th May 2026; Available online: 4th June 2026

1. Introduction

According to the International Energy Agency (IEA), more than 58 million Electric Vehicles (EVs) were operating worldwide in 2024, representing an increase of nearly 60% compared with the previous year (IEA, 2025). As the primary energy source for EVs, battery technology faces significant challenges in meeting relatively high and rapidly changing load-current demands. Such requirements are closely linked to the stop-and-go driving patterns characteristic of city traffic.

Currently, lithium-based batteries are considered the most suitable energy source for electric vehicles, offering efficiencies of approximately 80–95% (Lemian & Bode, 2022). Although lithium batteries remain the preferred choice for EV systems, their limited ability to handle high and rapidly changing currents can potentially degrade both their lifespan and performance (Vukajlović *et al.*, 2020). To accurately meet the load-current demands of EVs, an effective approach—beyond advancements in battery technology—is to supplement the power source with supercapacitors. Unlike batteries, supercapacitors possess a much higher power density, enabling them to deliver relatively high and rapidly changing currents. Furthermore, supercapacitors offer faster charge and discharge times compared to batteries, making them well-suited for handling peak current demands and supporting regenerative braking mechanisms (Itani *et al.*, 2016; Naseri *et al.*, 2017). Owing to their complementary characteristics, integrating batteries and supercapacitors as a hybrid power source (Batt–SC HPS) in EVs can enhance performance under diverse loading conditions. However, several factors must be addressed for its widespread adoption, including the relatively low energy density of supercapacitors, production costs, and infrastructure readiness (Huang *et al.*, 2019). Nevertheless, one study reported that employing Batt–SC technology as a hybrid power source in electric vehicles can achieve cost savings of approximately 12% compared to battery-only configurations (Song *et al.*, 2018). This finding highlights the significant potential of Batt–SC systems for future development and deployment, owing to their complementary power and energy characteristics.

Research on Batt–SC HPS technology continues to be an active and evolving field. Two major issues remain the focus of ongoing studies: dynamic modeling approaches and control strategies. Based on a comprehensive review, the dynamic model of a Batt–SC HPS typically comprises five state variables,

---

* Corresponding author
Email: arief.rohman@itb.ac.id (A. S. Rohman)

three controlled outputs, and two input signals (Al Tahtawi *et al.*, 2025a). Two modeling approaches have been proposed to represent Batt–SC HPS dynamics, including nonlinear models (Golchoubian & Azad, 2017; Mossadak *et al.*, 2024; Song *et al.*, 2017; Xu *et al.*, 2019) and a linearized model around the equilibrium point (Jung *et al.*, 2014; Zhao *et al.*, 2025; Zhong *et al.*, 2021). In addition to accurate modeling, Batt–SC HPS system must be governed by control strategies. Generally, two levels of control are employed in HPS configurations: high-level control (HLC), also referred to as the energy management system (EMS), and low-level control (LLC). The purpose of the HLC is to generate reference currents for each power source based on load conditions. This method is generally divided into four categories: rule-based (Khan *et al.*, 2018; Saw *et al.*, 2019; Zand *et al.*, 2020; Zheng *et al.*, 2017), filter-based (Maghfiroh *et al.*, 2024; Syahbana & Trilaksono, 2019), optimization-based (Abdelkader *et al.*, 2018; Amin *et al.*, 2014; Dao *et al.*, 2021), and learning-based (Abdelhedi *et al.*, 2018; Bourenane *et al.*, 2023; Udeogu & Lim, 2022). The selection among these approaches typically depends on system requirements such as control precision, adaptability to varying load conditions, and real-time implementation capability. However, some strategies—particularly optimization- and learning-based methods—can impose higher computational burdens, which may limit their practicality for embedded vehicle controllers or applications with strict real-time constraints. In contrast to HLC, the LLC is responsible for accurately tracking the reference currents generated by the HLC and regulating the DC bus voltage. LLC directly manages the dynamic behavior of the Batt-SC HPS system and its associated converters, ensuring fast response and stability under rapid load changes. In general, three main control approaches can be applied: classical control, optimal control, and robust control. Classical control includes methods such as proportional–integral (PI) control (Suthar *et al.*, 2024) and hysteresis control (Amin *et al.*, 2014). Optimal control encompasses techniques like linear quadratic control (Sadeq & Wai, 2020), model predictive control (MPC) (Syahbana & Trilaksono, 2019), and linear matrix inequality (LMI)-based optimization (Jung *et al.*, 2014; Zhong *et al.*, 2021). Meanwhile, robust control comprises strategies such as H_∞ control (Bai *et al.*, 2019), L2-gain control (X. Zhang *et al.*, 2021), backstepping control (Mossadak *et al.*, 2024), and sliding mode control (SMC) (Islam *et al.*, 2021; Xu *et al.*, 2019).

In practical operation, parameter variations in Batt–SC HPS system can occur due to several factors, including temperature fluctuations, component degradation, and load changes during vehicle operation. Parameters such as the internal resistance of the Batt–SC, the inductor resistance in the converter, and operating point variation may change over time, ultimately affecting control performance and system stability. Such variations can lead to discrepancies between the model used for controller design and the actual operating conditions. Therefore, mathematical modeling and control strategies that explicitly account for possible parameter variations in Batt–SC HPS must be properly addressed. In practical applications, the internal characteristics of the battery, supercapacitor, and its DC-DC converter can change over time due to aging, temperature fluctuations, and operating conditions. These variations directly affect the current–voltage response of the system and may lead to degraded performance or even instability if not considered in the control design. When considering parameter variations, both levels of control can be designed using a linear parameter-varying (LPV) control framework. At the HLC level, study (Larijani *et al.*, 2024) proposed an MPC for Batt–SC HPS based on an LPV model. This MPC-based EMS was developed by accounting for variations in Batt–SC voltages and their respective states of charge (SoC). However, for the LLC level, to the best of our knowledge, no prior studies have explicitly developed an LPV model for the Batt–SC HPS system nor formulated a corresponding control strategy capable of handling such variations. To address these challenges, the LPV framework can be employed, providing a systematic approach to represent nonlinear dynamics as linear systems with parameters varying within a known bounded set. Among LPV models, the polytopic-LPV representation stands out for its simplicity and suitability for controller synthesis using convex optimization techniques (Apkarian *et al.*, 1995).

Table 1
Comparison of the LLC-based control strategy for the Batt-SC HPS in the literature and the proposed controller in this work

Control strategies	Characteristics				References
	Dynamic model	Stability guarantee	L2-gain performance	Control input constraints	
PI controller	LTI	-	-	-	(Jia *et al.*, 2023; Larijani *et al.*, 2024)
Hysteresis control	LTI	-	-	-	(Amin *et al.*, 2014)
LQR	NTI	V	-	-	(Aini *et al.*, 2023; Sadeq & Wai, 2020)
MPC	NTI	V	-	-	(Syahbana & Trilaksono, 2019; Q. Zhang *et al.*, 2017)
LMI-based SF	LTI	V	V	V	(Jung *et al.*, 2014)
H_∞ controller	LTI	V	-	-	(Bai *et al.*, 2019)
L_2-gain passivity-based control	NTI	V	V	-	(X. Zhang *et al.*, 2021)
Back-stepping controller	NTI	V	-	-	(Mossadak *et al.*, 2024; Siffat *et al.*, 2020)
Sliding mode control (SMC)	NTI	V	-	-	(Ahmad *et al.*, 2024; Islam *et al.*, 2021; Song *et al.*, 2017; Suthar *et al.*, 2024; Xu *et al.*, 2019; X. Zhang *et al.*, 2023)
Robust MIMO LQR	LTI	V	-	-	(Zhao *et al.*, 2025)
Polytopic LMI-based SF	LPV	V	V	V	This work

NTI= Nonlinear Time-Invariant; LTI= Linear Time-Invariant; LPV= Linear Parameter-Varying

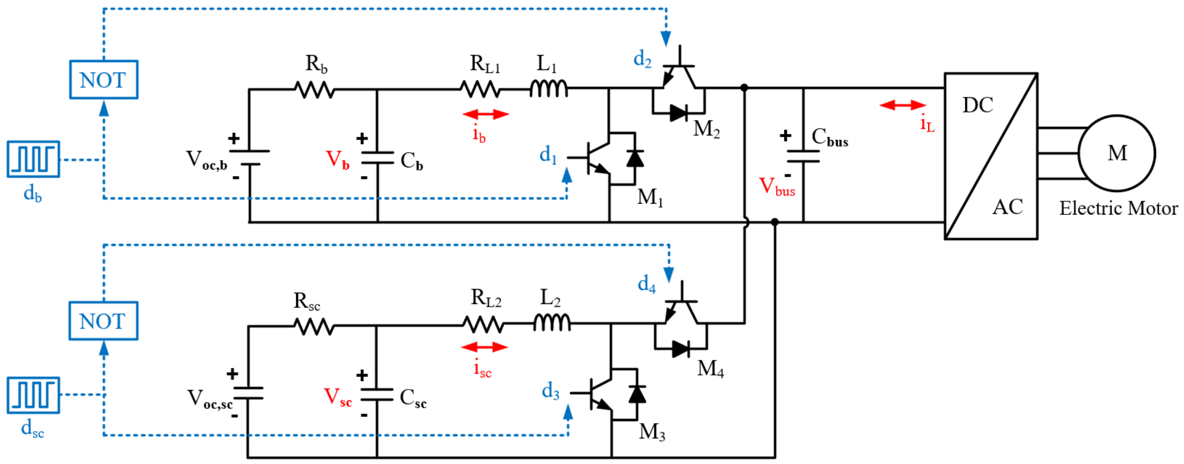

Fig. 1 Equivalent circuit model of Batt-SC HPS system with parallel bidirectional DC-DC boost converters. The blue parts represent system inputs in the form of duty cycles, and the red fonts are the system variables

In addition to addressing parameter variations, it is also necessary to consider the input constraints inherent in the Batt-SC HPS. This system relies on duty cycles, bounded between 0% and around 80%, to regulate the current flowing through the DC–DC boost converters on both the battery and supercapacitor sides. From the previously conducted stability analysis, it was observed that operating at or near a 100% duty cycle should be avoided, as this condition indicates a tendency for the system to lose stability (Al Tahtawi *et al.*, 2025b). Moreover, constraining the duty cycle is also important from an efficiency point of view. Practical DC–DC converters often exhibit optimal energy-conversion efficiency within a specific duty-cycle range, rather than at extreme values. Therefore, explicitly incorporating input constraints—particularly the allowable duty-cycle range—into the controller design is essential. This ensures not only the preservation of stability under various operating conditions but also the enhancement of efficiency and reliability of the Batt-SC HPS system.

Based on a literature review, Table 1 summarizes a comparative analysis of control strategies for the Batt–SC HPS, with emphasis on the adopted dynamic modeling approaches, stability guarantees, L2-gain performance, and control input constraints, as well as the research gap addressed by this work. To the best of the authors' knowledge, there has been no published work that explicitly models the Batt–SC HPS by considering parameter variations and simultaneously develops its LMI-based controller synthesis incorporating input constraints. Thus, the main contributions of this paper are summarized as follows:

- Development of a polytopic-LPV model for the Batt–SC HPS system, explicitly accounting for possible parameter variations.
- Synthesis of state-feedback control based on a set of simultaneous LMIs as a sufficient condition for the stability of the closed-loop Batt-SC HPS system, capable of guaranteeing Lyapunov quadratic stability and satisfying the L2-gain performance in the presence of parameter variations, while explicitly incorporating input constraints.

The rest of this paper is organized as follows. Section 2 presents the nonlinear Batt–SC HPS model, including the derivation of its equilibrium points, open-loop stability analysis, and linearized model. Section 3 describes the proposed control strategy, with particular emphasis on the synthesis of the state-feedback controller based on LMIs. Section 4 presents the numerical validation, simulation results, closed-loop stability analysis, and corresponding discussions. Finally, Section 5 concludes the paper and summarizes the main findings of this work.

2. System Model

2.1 Batt-SC HPS Nonlinear Model

The dynamic model of the Batt–SC HPS in fully active topology, shown schematically in Fig. 1, can be directly derived via Kirchhoff's laws. In a compact form, its dynamic equations can be formed into a nonlinear model expressed as

$$\dot{x}(t) = \mathcal{A}x(t) + \mathcal{B}(u,t)x(t) + \Gamma w(t) + \Omega \tag{1}$$

with $x(t) \in \mathbb{R}^5$ denotes state variable including battery voltage V_b, SC voltage V_{sc}, battery current i_b, SC current i_{sc}, and DC bus voltage V_{bus}, $u(t) \in \mathbb{R}^2$ denotes control signal in the form of duty cycle d_1 and d_3 for each bidirectional DC-DC boost converter, and $x(t) \in w(t) \in \mathbb{R}$ represents load current i_L as disturbance vector. The system matrices $\mathcal{A}$, $\mathcal{B}(u,t)$, Γ, and Ω are then defined as follows

$$\mathcal{A} = \begin{bmatrix} -\frac{1}{R_bC_b} & 0 & -\frac{1}{C_b} & 0 & 0 \\ 0 & -\frac{1}{R_{sc}C_{sc}} & 0 & -\frac{1}{C_{sc}} & 0A \\ \frac{1}{L_1} & 0 & -\frac{(R_{L1}+R_{ON2})}{L_1} & 0 & -\frac{1}{L_1} \\ 0 & \frac{1}{L_2} & 0 & -\frac{(R_{L2}+R_{ON4})}{L_2} & -\frac{1}{L_2} \\ 0 & 0 & \frac{1}{C_{bus}} & \frac{1}{C_{bus}} & 0 \end{bmatrix},$$

$$\mathcal{B}(u,t) = \begin{bmatrix} 0 & 0 & 0 & 0 & 0 \\ 0 & 0 & 0 & 0 & 0 \\ 0 & 0 & 0 & 0 & \frac{1}{L_1}u_1 \\ 0 & 0 & 0 & 0 & \frac{1}{L_2}u_2 \\ 0 & 0 & -\frac{1}{C_{bus}}u_1 & -\frac{1}{C_{bus}}u_2 & 0 \end{bmatrix},$$

$$\Gamma = \begin{bmatrix} 0 & 0 & 0 & 0 & -\frac{1}{C_{bus}} \end{bmatrix}^T, \ \Omega = \begin{bmatrix} \frac{V_{oc,b}}{R_bC_b} & \frac{V_{oc,sc}}{R_{sc}C_{sc}} & 0 & 0 & 0 \end{bmatrix}^T$$

with R_b, C_b, and $V_{oc,b}$ respectively are battery internal resistance, battery capacitance, and battery open-circuit voltage, R_{sc}, C_{sc}, and $V_{oc,sc}$ respectively are supercapacitor internal resistance, supercapacitor capacitance, and

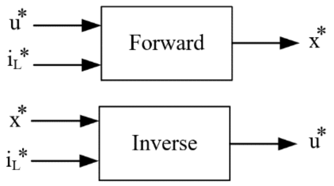

Fig. 2 Methods for equilibrium point computation

supercapacitor open-circuit voltage, L_1 and L_2 are inductance in each buck converter, R_{L1} and R_{L2} are resistance on each inductor, R_{ON2} and R_{ON4} are switching resistance on M_1/M_2 and M_3/M_4, and C_{bus} is capacitance in DC bus.

As can be seen, the Batt–SC HPS model in (1) exhibits nonlinear characteristics due to the multiplicative interaction between the states and the control inputs in $\mathcal{B}(u,t)$. Accordingly, for control design purposes, the model can be linearized around a selected operating point. In this context, the operating point is also referred to as an equilibrium point.

Remark 1: The dynamic model of the Batt–SC HPS in (1) was originally formulated as a sixth-order system, including the open-circuit voltage of the supercapacitor $V_{oc,sc}$ as a state variable. However, when addressing stabilization or tracking problems, it is necessary to define a valid equilibrium point (i.e., a point where the system can remain for a certain period of time). For control design, the controller for the fifth-order system remains valid for the sixth-order model over a sufficiently long time horizon. This is because variations in the $V_{oc,sc}$ occur much more slowly compared to the transient response of the other state variables.

2.2 Batt-SC HPS Equilibrium Point

In the Batt-SC HPS system, the equilibrium point represents the steady-state operating condition at which all state variables remain constant in the absence of external disturbances and reference variations. The equilibrium point serves as a nominal operating condition around which the nonlinear system dynamics can be linearized, enabling the application of linear or LPV-based control design techniques. To obtain the equilibrium point as the operating point of the system, two approaches can be employed: forward computation and inverse computation, as illustrated in Fig. 2.

In the forward computation method, the duty cycle is first selected as $u^* = [u_1^* \; u_2^*]^T = [d_1^* \; d_3^*]^T$ and the load current i_L^* is also specified as the desired operating point. With these values, the nonlinear model in (1) can be rewritten as follows

$$\dot{x}(t) = (\mathcal{A} + \mathcal{B})x(t) + \Phi \tag{2}$$

with $(\mathcal{A} + \mathcal{B})$ and $\Phi = \Gamma + w^*\Omega$ represent the new constant matrix and vector determined by the chosen operating points u_1^*, u_2^*, and i_L^*. For a given operating point, the equilibrium condition is obtained by setting $\dot{x}(t) = 0$. Consequently, the equilibrium point of state variables x^* can be calculated. The steady-state value x^* is then used as the operating point to derive the linearized system model around the equilibrium. The controlled variable can subsequently be determined as $y^* = \mathcal{C}x^*$, which represents the steady-state condition at which the controller operates. As noted in (Jung *et al.*, 2014) and (Zhong *et al.*, 2021), this procedure is referred to as converting a tracking problem into a stabilization problem. Nevertheless, tracking can still be performed, but only relative to the selected operating point.

Conversely, the equilibrium point can also be determined based on the desired values of the controlled outputs using an inverse computation approach. In this method, the steady-state values of the controlled variables are first specified, for example $y^* = [x_3^* \; x_5^*]^T = [i_b^* \; V_{bus}^*]^T$ along with i_L^*. Using this operating point, the duty cycles can then be obtained by solving the following set of algebraic equations

$$\begin{cases} V_{oc,b} - x_1^* - R_b x_3^* = 0 \\ V_{oc,sc} - x_2^* - R_{sc} x_4^* = 0 \\ x_1^* - (R_{L1} + R_{ON2})x_3^* - (1 - u_1^*)x_5^* = 0 \\ x_2^* - (R_{L2} + R_{ON4})x_4^* - (1 - u_2^*)x_5^* = 0 \\ (1 - u_1^*)x_3^* + (1 - u_2^*)x_4^* - i_L^* = 0 \end{cases} \tag{3}$$

This equation (3) represents a simplified form of the nonlinear Batt-SC HPS model in (1) evaluated at steady state, i.e., when $\dot{x}(t) = 0$. However, applying this approach requires slightly more involved mathematical manipulation compared with the forward method in. This is due to the presence of several unknown variables, such as x_1^*, x_2^*, and x_4^*, which necessitate repeated linear substitutions and solving quadratic expressions. The advantage of this method is that the desired operating specifications of the system can be explicitly prescribed, and the resulting control inputs will naturally operate around the computed u^*.

2.3 Batt-SC HPS Stability

The stability of the Batt–SC HPS system can be analyzed using a polytopic modeling approach. As shown in (1), the presence of the input variable $u(t)$ in the matrix $\mathcal{B}$ allows the characterization of all possible system dynamics with respect to variations in the input $u(t)$. Furthermore, a sufficient condition for the open-loop stability of the Batt–SC HPS can be expressed in the form of an LMI, as stated in Proposition 1.

Proposition 1 (Batt-SC HPS open-loop stability): If there exists a positive definite matrix $P = P^T > 0$ and a positive L2-gain constant $\gamma > 0$ such that

$$\begin{bmatrix} \mathcal{A}_{poly}^{(m,n)^T} P + P\mathcal{A}_{poly}^{(m,n)} & * & * \\ \Gamma^T P & -\gamma I & * \\ \mathcal{C} & 0 & -\gamma I \end{bmatrix} < 0 \tag{4}$$

for $m = 1, 2, \ldots, M; n = 1, 2, \ldots, N; (m,n) \neq (M,N)$, the Batt-SC HPS open-loop system (1) is stable for all duty cycle input combinations.

Proof: See (Al Tahtawi *et al.*, 2025b).

The simultaneous LMIs in (4) can be computed by assigning the system dynamic parameters to the matrices $\mathcal{A}$ and Γ, and by defining the matrix $\mathcal{C}$ to represent the outputs i_b and V_{bus}. The matrix $\mathcal{A}_{poly}^{(m,n)}$ denotes the polytopic representation of the system matrix $\mathcal{A} + \mathcal{B}(u)$, which captures all possible system dynamics resulting from combinations of the input duty cycle $u \in [0,1]$. Meanwhile, γ represents the L2-gain constant that characterizes the boundedness of the system output in the presence of the load current i_L as an external disturbance.

A key aspect of the sufficient stability condition is the exclusion of the matrix $\mathcal{A}_{poly}^{(m,n)}$ corresponding to the case $(m,n) = (M,N)$. This condition represents the extreme input combination in which both DC–DC boost converters operate at a 100% duty cycle. Including this operating point leads to an order reduction of the dynamic model in (1), rendering the LMI in (4) infeasible. From a practical perspective, this condition is consistent with the inherent characteristics of DC-DC boost

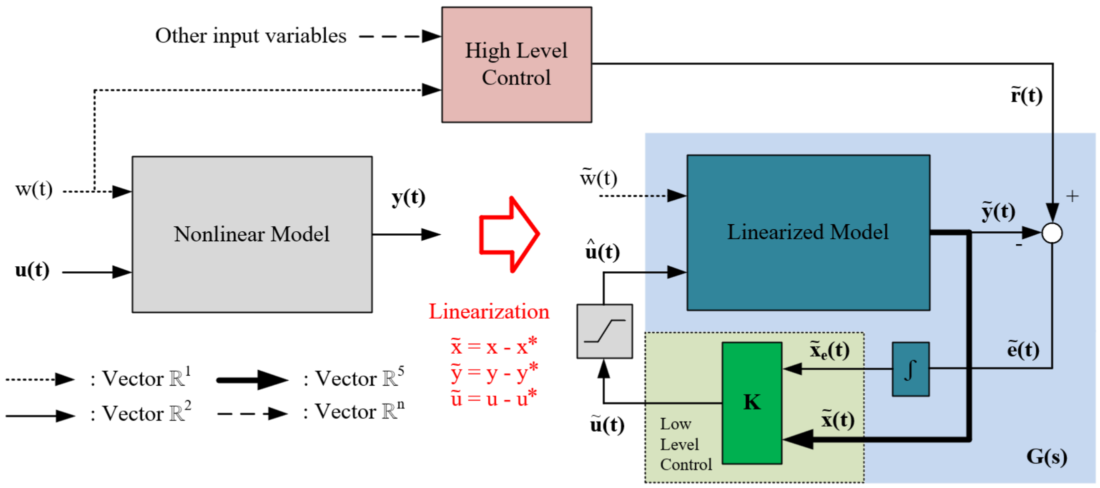

Fig. 3 State-feedback control design for the linearized model of the Batt-SC HPS system

converters, where operation at a 100% duty cycle results in unbounded responses of both i_b and V_{bus}. Consequently, this input condition, or values approaching it, must be avoided in practical operation (the maximum allowable duty cycle is typically around 80%).

2.4 Batt-SC HPS Linearized Model

For the controller synthesis, the nonlinear model (1) can be linearized around its equilibrium point. Let $\tilde{x} = x - x^*$, $\tilde{u} = u - u^*$, $\tilde{y} = y - y^*$, and $\tilde{w} = w - w^*$ denote as new variables. The linear model with an output can be derived as

$$\begin{cases}\dot{\tilde{x}}(t) = A\tilde{x}(t) + B\tilde{u}(t) + \Gamma\tilde{w}(t) \\ \tilde{y}(t) = C\tilde{x}(t)\end{cases} \tag{5}$$

with

$$A = \frac{\partial f}{\partial x}(x^*, u^*) =$$

$$\begin{bmatrix} -\frac{1}{R_bC_b} & 0 & -\frac{1}{C_b} & 0 & 0 \\ 0 & -\frac{1}{R_{sc}C_{sc}} & 0 & -\frac{1}{C_{sc}} & 0 \\ \frac{1}{L_1} & 0 & -\frac{(R_{L1}+R_{ON2})}{L_1} & 0 & -\frac{1}{L_1}(1-u_1^*) \\ 0 & \frac{1}{L_2} & 0 & -\frac{(R_{L2}+R_{ON4})}{L_2} & -\frac{1}{L_2}(1-u_2^*) \\ 0 & 0 & \frac{1}{C_{bus}}(1-u_1^*) & \frac{1}{C_{bus}}(1-u_2^*) & 0 \end{bmatrix},$$

$$B = \frac{\partial f}{\partial u}(x^*, u^*) = \begin{bmatrix} 0 & 0 & \frac{1}{L_1}x_5^* & 0 & -\frac{1}{C_{bus}}x_3^* \\ 0 & 0 & 0 & \frac{1}{L_2}x_5^* & -\frac{1}{C_{bus}}x_4^* \end{bmatrix},$$

$$C = \begin{bmatrix} 0 & 0 & 1 & 0 & 0 \\ 0 & 0 & 0 & 0 & 1 \end{bmatrix}$$

Since the system involves a non-zero setpoint, an additional state variable is introduced to represent the integral of the tracking error, defined as follows

$$\tilde{x}_e(t) = \int(\tilde{r}(t) - \tilde{y}(t))\ dt = \int(\tilde{r}(t) - C\tilde{x}(t))\, dt \tag{5}$$

Furthermore, the new linear model can be obtained with new state variables

$$\xi(t) = \begin{bmatrix}\tilde{x} \\ \tilde{x}_e\end{bmatrix} = \begin{bmatrix}\tilde{V}_b & \tilde{V}_{sc} & \tilde{\imath}_b & \tilde{\imath}_{sc} & \tilde{V}_{bus} & \int \tilde{e}_{i_b} & \int \tilde{e}_{V_{bus}}\end{bmatrix}^T$$

and references

$$\tilde{r} = \begin{bmatrix}\tilde{\imath}_{bref} & \tilde{V}_{busref}\end{bmatrix}^T$$

as follows

$$\begin{cases}\dot{\xi}(t) = \hat{A}\xi(t) + \hat{B}\tilde{u}(t) + \hat{\Gamma}\tilde{w}(t) + \Psi\tilde{r}(t) \\ \tilde{y}(t) = \hat{C}\xi(t)\end{cases} \tag{6}$$

where $\hat{A} = \begin{bmatrix} A & 0_{5\times2} \\ -C & 0_{2\times2}\end{bmatrix}$, $\hat{B} = \begin{bmatrix} B \\ 0_{2\times2}\end{bmatrix}$, $\hat{C} = [C \quad 0_{2\times2}]$, $\hat{\Gamma} = \begin{bmatrix}\Gamma \\ 0_{2\times1}\end{bmatrix}$, and $\Psi = \begin{bmatrix}0_{5\times2} \\ I_{2\times2}\end{bmatrix}$.

Remark 2: The controller designed based on the linearized model around the selected equilibrium point guarantees stability and performance only locally. It operates when the Batt–SC HPS is at the chosen operating point and responds to disturbances $\tilde{w}(t)$ or reference tracking commands $\tilde{r}(t)$ in the vicinity of that equilibrium.

2.5 Batt-SC HPS Polytopic Model

Based on the linearized model (6), the polytopic model of the Batt-SC HPS can be expressed by incorporating the time-varying parameter θ into the system matrices. Accordingly, we obtain the matrices where $\hat{A}(\theta)$, $\hat{B}(\theta)$, $\hat{C}(\theta)$, $\hat{\Gamma}(\theta)$, and $\Psi(\theta)$. The vertex models, which represent the extreme points of the convex hull, can be defined as

$$\Lambda(\theta) \in \mathbb{P} \coloneqq \mathrm{Co}\,\{\Lambda_i :\ i = 1,2,\dots,k\} \tag{7}$$

or equivalently

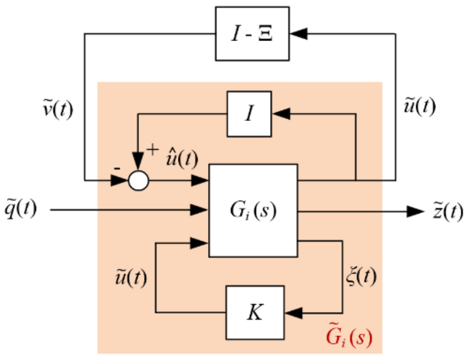

Fig. 4 Modified generalized plant scheme incorporating deadzone nonlinearity

$$\Lambda(\theta) = \sum_{i=1}^{k} \alpha_i \Lambda_i \quad (8)$$

with $\Lambda := \begin{bmatrix} \hat{A} & \hat{B} & \hat{\Gamma} & \Psi \\ \hat{C} & 0 & 0 & 0 \end{bmatrix}$, $\alpha_i \geq 0$, and $\sum_{i=1}^{k} \alpha_i = 1$.

In the Batt–SC HPS linearized model, only the matrices $\hat{A}$, $\hat{B}$, and $\hat{\Gamma}$ contain elements that explicitly depend on the varying parameters, and therefore, these matrices exhibit time-varying characteristics. If all parameter variations are included in each matrix, then the total number of system vertices becomes $k = 2^{17} = 131{,}072$. The selection of varying parameters may be based on design requirements or may refer to sensitivity analysis of the system output. In general, the more parameters considered as varying, the larger the number of system vertices, resulting in higher computational cost in controller synthesis.

3. Control Synthesis

The controller is synthesized based on a linearized model around the selected equilibrium point, as shown in Fig. 3. The objective of this controller is to regulate or track the battery current generated by the HLC and also to regulate the DC bus voltage at the same time, while ensuring system stability in the presence of parameter variations and input saturation. The controller is synthesized to guarantee closed-loop stability while satisfying L2-gain performance and sector nonlinearity. The system vertices are then utilized to formulate the set of simultaneous LMIs based on quadratic Lyapunov stability (Boyd *et al.*, 1994). The generalized model is employed to facilitate the control design process by simplifying the relationships among system variables, as illustrated in Fig. 4. In this generalized representation, the linearized model of the Batt–SC HPS around the equilibrium point can be represented by the vertex model $G_i(s)$, which is expressed in the form of a transfer function matrix

$$G_i(s) := \hat{C}_i \left(sI - \hat{A}_i\right)^{-1} \hat{B}_i;\ i = 1, 2, \dots, k \quad (9)$$

In this study, the sector nonlinearity technique is selected, as it guarantees system stability for all nonlinearities that lie within the defined sector. The nonlinearity considered in this case is the actuator saturation. Consequently, the control input applied to $G_i(s)$ is defined as

$$\Xi\tilde{u}(t) = \begin{cases} \tilde{u}_{max}(t), & \tilde{u}(t) > \tilde{u}_{max}(t) \\ \tilde{u}(t), & \tilde{u}(t) \in [-\tilde{u}_{min}(t), \tilde{u}_{max}(t)] \\ -\tilde{u}_{min}(t), & \tilde{u}(t) < -\tilde{u}_{min}(t) \end{cases} \quad (10)$$

where Ξ is a diagonal saturation operator. Since the Batt-SC HPS system has two control inputs $\tilde{u}(t) = [\tilde{u}_1(t) \quad \tilde{u}_2(t)]^T = [\tilde{d}_1(t) \quad \tilde{d}_3(t)]^T$, the saturation operator can be expressed as

$$\Xi := \begin{bmatrix} sat_1 & 0 \\ 0 & sat_2 \end{bmatrix} \quad (11)$$

where sat_1 represents the saturation applied to $\tilde{u}_1(t)$, and sat_2 corresponds to the saturation of $\tilde{u}_2(t)$. To enhance the convexity in finding a feasible LMI solution, the generalized model $G_i(s)$ is modified by reformulating the saturation nonlinearity into a deadzone nonlinearity represented by $I - \Xi$. By adding the control signal $\tilde{u}(t)$ to the model $G_i(s)$, the resulting nonlinearity recovers the saturation form (Mulder *et al.*, 2015). For instance, the deadzone function on the control signal can be defined as follows

$$\tilde{v} := I\tilde{u} - \Xi(\tilde{u}) \quad (12)$$

Consequently, the new generalized model $\tilde{G}_i(s)$ involves sector nonlinearity in the form of saturation $\hat{u}(t) = sat(\tilde{u}(t))$ with a state-feedback control law

$$\tilde{u}(t) = K\xi(t) \quad (13)$$

can be expressed as follows

$$\begin{cases} \dot{\xi} = \left(\hat{A}_i + \hat{B}_i K\right)\xi - \hat{B}_i \tilde{v} + \Upsilon_i \tilde{q} \\ \tilde{z} = \hat{C}_{z,i}\xi + D_i \tilde{q} \end{cases};\ i = 1, 2, \dots, k \quad (14)$$

with $\tilde{q} = \begin{bmatrix} \widetilde{W} \\ \tilde{r} \end{bmatrix}$, $\tilde{z} = \begin{bmatrix} \tilde{y} \\ \tilde{e} \end{bmatrix}$, $\Upsilon = [\hat{\Gamma} \quad \Psi]$, $\hat{C}_z = \begin{bmatrix} \hat{C} \\ -\hat{C} \end{bmatrix}$, and $D = \begin{bmatrix} 0_{2\times1} & 0_{2\times2} \\ 0_{2\times1} & I_{2\times2} \end{bmatrix}$.

Remark 3: The generalized model (14) is then required to be open-loop stable (Lur'e problem).

The state-feedback controller is synthesized to achieve three objectives: (1) to stabilize the battery current and the DC bus voltage in the presence of load current fluctuation; (2) to track the battery current reference while simultaneously stabilizing the DC bus voltage under constant load current; and (3) to track the battery current and stabilize the DC bus voltage during load current variations. These control objectives are synthesized based on a common Lyapunov stability framework augmented with exponential decay rate μ, L2-gain performance criterion, and sector nonlinearities, as follows

$$\dot{\xi}^T P\xi + \xi^T P\dot{\xi} + 2\mu\xi^T P\xi + \gamma^{-1}\tilde{z}^T\tilde{z} - \gamma\tilde{q}^T\tilde{q} + 2\tilde{v}^T W(\tilde{u} - \tilde{v}) < 0 \quad (15)$$

As a result, the controller formulation can be expressed as a simultaneous LMI-based minimization problem as follows.

Proposition 2 (State-feedback controller synthesis): A state-feedback controller that guarantees the stability of the polytopic Batt–SC HPS system for stabilizing, tracking, and tracking with stabilizing can be obtained if there exists a positive definite matrix $X = X^T > 0$ that satisfies these minimization problems

$$\min_{X,Q,W,\mu} \gamma \ \text{ s.t.}$$

$$\begin{bmatrix} \text{He}\left(X\hat{A}_i^T + \hat{B}_i Q\right) + 2\mu X & * & * & * \\ -\hat{B}_i^T + Y & -2W & * & * \\ \hat{\Gamma}_i^T & 0 & -\gamma I & * \\ \hat{C}_i X & 0 & 0 & -\gamma I \end{bmatrix} < 0 \quad (16)$$

$$\begin{bmatrix} \text{He}\left(X\hat{A}_i^T + \hat{B}_i Q\right) + 2\mu X & * & * & * \\ -\hat{B}_i^T + Y & -2W & * & * \\ \Psi_i^T & 0 & -\gamma I & * \\ \hat{C}_i X & 0 & -I & -\gamma I \end{bmatrix} < 0 \quad (17)$$

$$\begin{bmatrix} \text{He}\left(X\hat{A}_i^T + \hat{B}_i Q\right) + 2\mu X & * & * & * \\ -\hat{B}_i^T + Y & -2W & * & * \\ \Upsilon_i^T & 0 & -\gamma I & * \\ \hat{C}_{z,i} X & 0 & D_i & -\gamma I \end{bmatrix} < 0 \quad (18)$$

for $i = 1, 2, \dots, k$

Proof: Substituting the closed-loop generalized model (14) into inequality (15) yields the following expression for each vertex

$$\begin{aligned} \xi^T \hat{A}_i^T P\xi + \xi^T K^T \hat{B}_i^T P\xi - \tilde{v}^T \hat{B}_i^T P\xi + \tilde{q}^T \Upsilon_i^T P\xi + \xi^T P\hat{A}_i \xi \\ + \xi^T P\hat{B}_i K\xi^T - \xi^T P\hat{B}_i \tilde{v} + \xi^T P\Upsilon_i \tilde{q} + 2\mu\xi^T P\xi \\ + \gamma^{-1}\xi^T \hat{C}_{z,i}^T \hat{C}_{z,i}\xi + 2\gamma^{-1}\xi^T \hat{C}_{z,i}^T D_i \tilde{q} \\ + \gamma^{-1}\tilde{q}^T D_i^T D_i \tilde{q} - \gamma\tilde{q}^T\tilde{q} + 2\tilde{v}^T WK\xi \\ - 2\tilde{v}^T W\tilde{v} < 0 \end{aligned} \quad (19)$$

For $[\xi \quad \tilde{v} \quad \tilde{q}]^T \neq 0$, the inequality (19) can be written in the following LMI form

$$\begin{bmatrix} \mathrm{He}\left(\hat{A}_i^T P + K^T \hat{B}_i^T P\right) + 2\mu P + \gamma^{-1}\hat{C}_{z,i}^T \hat{C}_{z,i} & * & * \\ -\hat{B}_i^T P + WK & -2W & * \\ \Upsilon^T P + \gamma^{-1}\hat{C}_{z,i}^T D_i & 0 & \gamma^{-1} D_i^T D_i - \gamma I \end{bmatrix} < 0 \tag{20}$$

Let us define a new variable

$$\varepsilon = \begin{bmatrix} \gamma^{-1}\hat{C}_{z,i}^T \hat{C}_{z,i} & * & * \\ 0 & 0 & * \\ \gamma^{-1}\hat{C}_{z,i}^T D_i & 0 & \gamma^{-1} D_i^T D_i - \gamma I \end{bmatrix} \tag{21}$$

which can be expressed as

$$\varepsilon = \begin{bmatrix} 0 & * & * \\ 0 & 0 & * \\ 0 & 0 & -\gamma I \end{bmatrix} + \begin{bmatrix} \hat{C}_{z,i}^T \\ 0 \\ D_i^T \end{bmatrix} (\gamma I)^{-1} \begin{bmatrix} \hat{C}_{z,i} & 0 & D_i \end{bmatrix} \tag{22}$$

Therefore, the LMI (20) can be reformulated as follows

$$\begin{bmatrix} \mathrm{He}\left(\hat{A}_i^T P + K^T \hat{B}_i^T P\right) + 2\mu P & * & * \\ -\hat{B}_i^T P + WK & -2W & * \\ \Upsilon^T P & 0 & 0 \end{bmatrix} + \varepsilon < 0 \tag{23}$$

By applying Schur complement, defining $X = P^{-1}$, $Q = KX$, and $Y = WQ$, also performing a pre- and post-multiplications with diag (X, I, I, I), the LMI (18) is established. LMIs (16) and (17) can also be derived by decomposing the vectors $\tilde{q}$ and $\tilde{z}$ according to the L2-gain criteria for stabilization ($\tilde{q} = \tilde{w}, \tilde{z} = \tilde{y}$) and tracking ($\tilde{q} = \tilde{r}, \tilde{z} = \tilde{e}$). The proof is completed.

4. Numerical Simulation Result

As an example, consider that parameter variations arise from changes in internal resistance due to temperature fluctuations during operation. The variation of internal resistance is selected as a case study because it represents one of the most significant and practical sources of parameter uncertainty in Batt-SC HPS systems, particularly due to temperature changes, aging effects, and varying operating conditions. In the linear dynamic model (6), four resistances are assumed to vary, denoted by ΔR_b, ΔR_{sc}, ΔR_{DC1}, and ΔR_{DC2}. Here, ΔR_b and ΔR_{sc} represent variations in the internal resistances of the battery and supercapacitor, respectively, while ΔR_{DC1} and ΔR_{DC2} denote variations in the internal resistances of each DC-DC converter, including inductor and switching resistances. Since in the model (6) the values of R_b and R_{sc} appear inversely in the parameter-varying matrix $\hat{A}$, the internal conductances of the Batt-SC system are defined as $G_b = 1/R_b$ and $G_{sc} = 1/R_{sc}$. Because four parameters vary with time, the number of $\hat{A}$-matrix vertices becomes $k = 2^4 = 16$, which can be written as

$$\hat{A}(\theta) = \mathrm{Co}\left\{\hat{A}_1, \hat{A}_2, \ldots, \hat{A}_{16}\right\} = \textstyle\sum_{i=1}^{16} \alpha_i \hat{A}_i \tag{24}$$

where each vertex corresponds to the extreme values (minimum/maximum) of the internal resistances. The convex weights can be computed using linear interpolation as follows

$$\alpha_i = \textstyle\prod_{j=1}^{4} \left(1 - \theta_j\right)^{(i)}; i = 1, 2, \ldots, 16 \tag{25}$$

Let $\beta_j = [\beta_1 \quad \beta_2 \quad \beta_3 \quad \beta_4]$ denote the vector of varying parameters, where each β_j represents G_b, G_{sc}, R_{DC1}, and R_{DC2}. The normalized weights associated with the system vertices can be calculated as follows

$$\theta_j = \frac{\beta_j - \beta_j^{min}}{\beta_j^{max} - \beta_j^{min}}; i = 1, 2, 3, 4 \tag{26}$$

The time-varying parameters $\theta(t)$ are therefore constrained to the interval [0,1] by θ_j and are used to represent the convex combination of vertex systems in the polytopic-LPV model of the Batt-SC HPS. This formulation can also be conducted under various other parameter variation scenarios.

Numerical validation is performed to determine the feasibility of the solution of the simultaneous LMI formulations presented in Proposition 2. The LMI computations are performed using the LMI solver 'mincx' available in MATLAB. To further validate the LMI computation results, closed-loop simulations are also conducted for each control scheme. The evaluation is performed by applying the controller gain matrix K obtained from each LMI to several system vertices. Due to the large number of vertices, the closed-loop simulations are conducted on vertex 1, vertex 16, and on parameter values located between these vertices. The parameters of the Batt-SC HPS system for a load scale of approximately 1 kW are presented in Table 2.

For controller computation, the parameter variations are defined as $2\mho < G_b < 10\mho$, $20\mho < G_{sc} < 100\mho$, $0.1\mho < R_{DC1} < 0.5\mho$, and $0.1\mho < R_{DC2} < 0.5\mho$. Vertex 1 represents the Batt-SC HPS model when all parameters are at their minimum values, while vertex 16 corresponds to the model when the parameters reach their maximum values. Meanwhile, the parameter values selected between these two vertices correspond to the nominal values listed in Table 2. Before conducting the numerical validation and simulation, the system's operating point at which the controller will function must first be determined. For simplicity, the operating point is selected based on the forward computation method with $u^* = [u_1^* \quad u_2^*]^T = [d_1^* \quad d_3^*]^T = [0.5 \quad 0.5]^T$ and the load current $i_L^* = 10A$. The selection of the operating point can be adjusted according to system requirements, as long as the duty cycle remains within the allowable range. It is worth noting that the closer the operating duty cycle is to its minimum or maximum limit, the more the system can be regarded as operating under extreme conditions.

Based on the chosen operating point, the system output equilibrium point is obtained $y^* = [i_b^* \quad V_{bus}^*]^T = [7.4606 \quad 90.6582]^T$. This equilibrium point is then used as the operating point at which the linear control of the system is operated. The obtained state-feedback gain K, derived from the LMIs (16), (17), and (18) with $\mu = 10$, along with the corresponding values of W and γ, are presented as follows

Controller 1 stabilization scheme:

$$K = 10^3 \begin{bmatrix} -0.0961 & -0.0563 \\ 0.0004 & 0.0002 \\ -1.3241 & -0.6727 \\ -1.8354 & -0.9938 \\ -0.1735 & -0.0716 \\ -6.5497 & -4.2199 \\ 5.8841 & 2.9062 \end{bmatrix}^T, W = \mathrm{diag}(115.0608),$$

$\gamma = 7.9882$

Controller 2 tracking scheme:

$$K = 10^4 \begin{bmatrix} -0.0075 & -0.0118 \\ 0.0000 & 0.0000 \\ -0.1899 & -0.2508 \\ -0.2585 & -0.3700 \\ -0.0102 & -0.0074 \\ -1.7757 & -3.0941 \\ 0.7762 & 1.0731 \end{bmatrix}^T, W = \mathrm{diag}(61.6888),$$

$\gamma = 2.8800$

Controller 3 tracking with stabilization scheme:

Table 2
Batt-SC HPS nominal parameter for simulation

Parameters	Values	Units
Batt-SC initial voltage ($V_{oc,b} = V_{oc,sc}$)	48	V
Battery internal resistance (R_b)	0.237	Ohm
SC internal resistance (R_{sc})	0.012	Ohm
Battery filter capacitance (C_b)	10	mF
SC filter capacitance (C_{sc})	400	uF
Battery-side inductor (L_1)	40	mH
SC-side inductor (L_2)	36	mH
L1 resistance (R_{L1})	0.2	Ohm
L2 resistance (R_{L2})	0.16	Ohm
Switching resistance (R_{ON})	0.021	Ohm
Capacitor bus (C_{bus})	1	mF

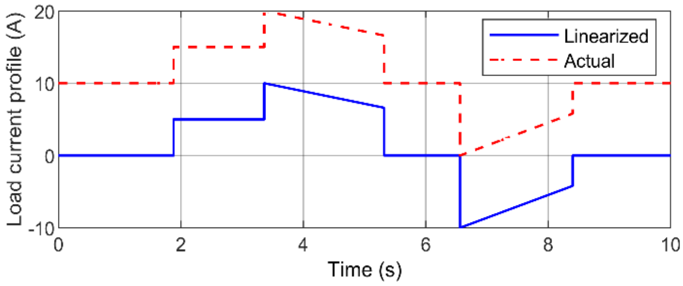

Fig. 5 Load current profile for system testing

$$K = 10^4 \begin{bmatrix} -0.0140 & -0.0083 \\ 0.0001 & 0.0000 \\ -0.1930 & -0.1024 \\ -0.2719 & -0.1514 \\ -0.0304 & -0.0144 \\ -1.0502 & -0.6695 \\ 1.0129 & 0.5289 \end{bmatrix}^T, W = \text{diag}(106.3309),$$

$$\gamma = 9.3937$$

The computational complexity of the proposed LMI optimization increases with the number of polytopic vertices; however, since the controller synthesis is performed offline, the resulting computational burden does not affect the real-time implementation of the proposed control strategy. The designed controller operates on the linearized model when the system is active and at its equilibrium point, as described in Remark 2. The load current profile for system testing, considered as the disturbance as well as the deviation from the equilibrium point, is shown in Fig. 5. The disturbance profile is designed as a combination of pulse and ramp signals with an amplitude of $\pm 10A$. This profile represents an instantaneous current demand experienced by the Batt-SC HPS when operating at its equilibrium point. Other load current profiles can also be applied, such as those derived from the standard EUDC, NEDC, or WLTP speed profiles.

4.1 Simulation Result for Stabilization Scheme

In control scheme 1, the closed-loop system test is carried out to stabilize the system output while minimizing the performance constant γ. The controller gain is then applied to the closed-loop system to minimize the effect of the load current fluctuation as a disturbance on the system output at its equilibrium point when $\tilde{r}(t) = 0$. The control input in the form of a duty cycle is then constrained to $u(t) \in [0,0.8]$. Then, the resulting output response of the actual system is presented in Fig. 6(a), and the resulting control signal is shown in Fig. 7(a). The test results indicate that the controller is capable of stabilizing the closed-loop system when subjected to system vertices and load current disturbance at the equilibrium point. The battery current and DC bus voltage are able to return to their operating points, although there is a high overshoot up to 287.66%. These responses are observed for vertex 1, vertex 16, as well as for parameters between the vertices (current sys). The large overshoot observed in the stabilization scheme mainly occurs during the initial transient response due to the significant difference between the initial condition and the equilibrium point used for stabilization. In this work, the stabilization scenario is primarily intended to evaluate the feasibility and robustness of the proposed controller under parameter variations and input saturation constraints rather than to represent a practical EV operating condition. Although the percentage overshoot appears high, the system response remains bounded and rapidly converges to the desired equilibrium point without violating the actuator saturation limits. Therefore, the transient behavior does not compromise the closed-loop stability of the system. The performance of the resulting response also depends on the selection of the parameter μ in the LMI. A smaller value *of* μ leads to a smaller overshoot, but results in a slower transient response toward the equilibrium point. Conversely, increasing μ accelerates the transient response by shifting the dominant closed-loop poles further into the left-half complex plane, at the expense of increased overshoot and higher control effort. Therefore, the choice of μ represents a trade-off between transient speed, damping characteristics, and control signal magnitude. For completeness, the supercapacitor current is also presented. It can be seen that the supercapacitor responds to the load current demand while the battery current is maintained at its operating point. This response indicates that the hybridization of the power sources behaves as expected.

For the control signal, it can be observed that a significant overshoot occurs when the disturbance takes place. This happens because the controller gain obtained from the LMI formulation accounts for the minimization of γ, resulting in

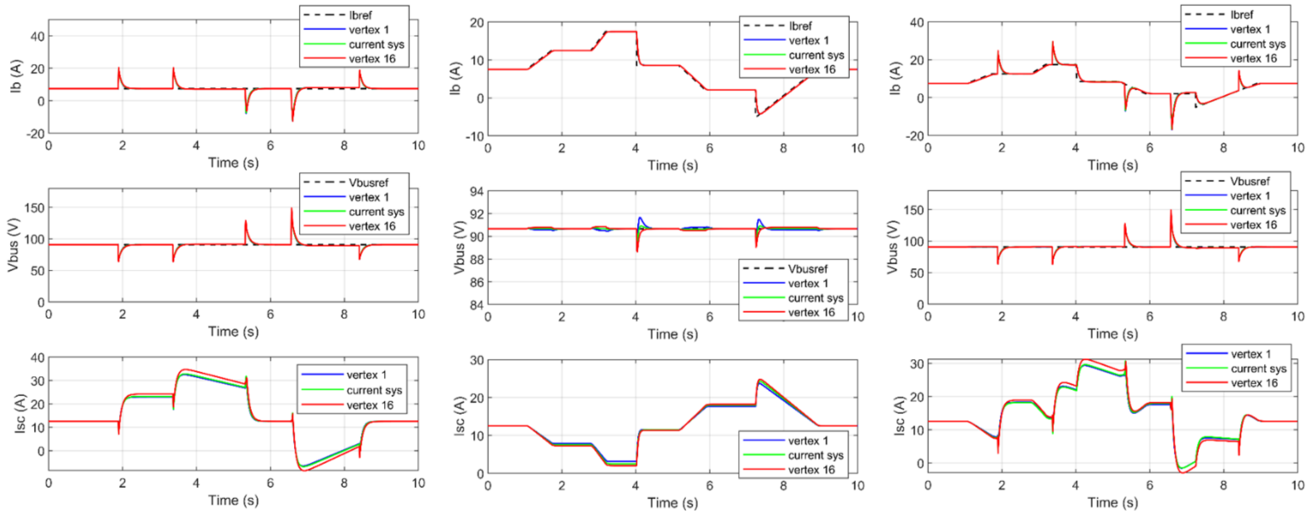

(a) (b) (c)

Fig. 6 Responses of battery current, DC bus voltage, and SC current under three control schemes: (a) stabilization, (b) tracking, and (c) tracking with stabilization

larger control signals. The largest control signal surge occurs at vertex 16, even though it does not exceed the specified saturation limits $u(t) \in [0,0.8]$. This condition represents the extreme operating point of the closed-loop system in handling disturbances.

4.2 Simulation Result for Tracking Scheme

The control scheme 2 is synthesized to minimize γ, thereby ensuring tracking capability. The system output responses for $\tilde{r}(t)$, where the battery current reference varies by $\pm 10A$ around the equilibrium point and the DC bus voltage reference is set to zero or at the operating point, are shown in Fig. 6(b). The results indicate that the battery current is able to track the reference signal for both the tested vertices and parameter values between the vertices. Similarly, the DC bus voltage overshoot during reference changes is smaller, reaching 2.39% at vertex 16. Unlike in the stabilization scheme, in this tracking scheme, the supercapacitor current responds in the opposite direction to the battery current. This occurs because, in this scenario, the load current is assumed to remain constant.

The resulting control signals are shown in Fig. 7(b). In this case, the generated control signal does not exceed the prescribed saturation limits $u(t) \in [0,0.8]$. It can be observed that control signal overshoot occurs at the moments of reference changes. Although the control input overshoot produced is relatively smaller compared to scheme 1, larger reference values may lead to higher overshoot. Therefore, limiting the control signal amplitude is essential to ensure reliable and efficient operation, especially for a DC-DC converter.

4.3 Simulation Result for Tracking with Stabilization Scheme

In this final scheme, the controller is designed to simultaneously track the reference and minimize the disturbance effects caused by load current fluctuations. The controller is obtained by minimizing a common γ for both L2-gain criteria. The resulting responses are presented in Fig. 6(c). The simulation results demonstrate a combined tracking and disturbance stabilization performance. The controller is able to track the battery current reference and regulate the DC bus voltage, although overshoots occur during load current fluctuations. It is also observed that the supercapacitor current responds in a complementary manner during battery current tracking while simultaneously compensating for the load current variations.

The corresponding control signals generated under this scheme are shown in Fig. 7(c). It can be observed that the control signals represent a combination of the tracking and stabilization schemes. Similar high overshoots occur during load current fluctuations, as observed in the stabilization scheme. Nevertheless, the imposed saturation effectively limits the

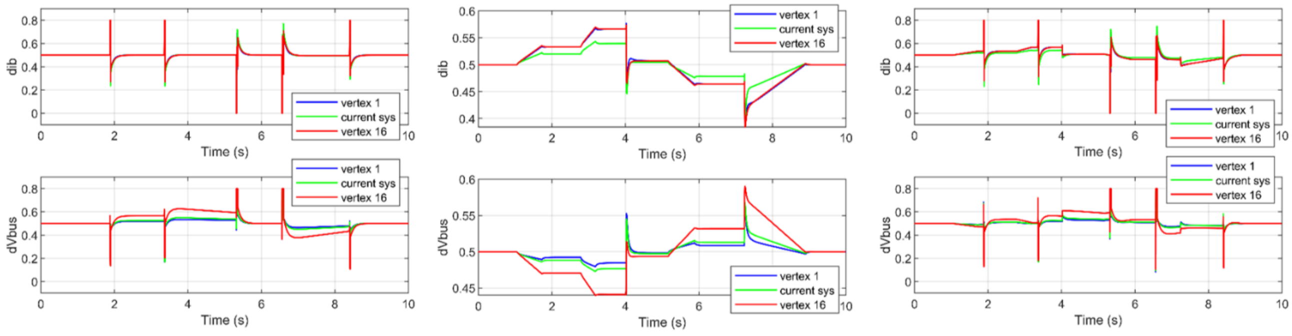

(a) (b) (c)

Fig. 7 Control signals under three control schemes: (a) stabilization, (b) tracking, and (c) tracking with stabilization

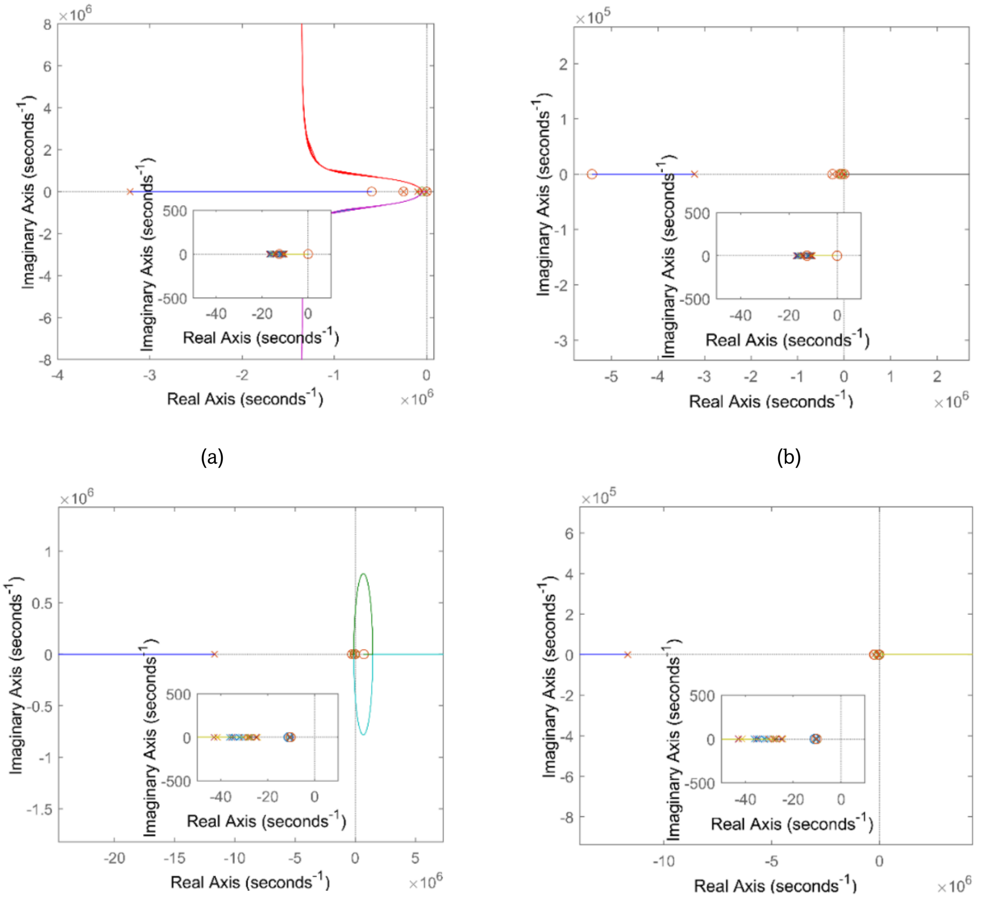

(a)

(b)

(c)

(d)

Fig. 8 Closed-loop eigenvalues at all vertices in stabilization and tracking schemes: (a) from $\tilde{w}(t)$ to $\tilde{y}_1(t)$, (b) from $\tilde{w}(t)$ to $\tilde{y}_2(t)$, (c) from $\tilde{r}_1(t)$ to $\tilde{y}_1(t)$, (d) from $\tilde{r}_2(t)$ to $\tilde{y}_2(t)$

excessive control signal amplitudes. This saturation mechanism plays a crucial role in preventing unrealistic or unsafe control actions, thereby ensuring the practical implementation of the proposed controller in real power electronic systems. Moreover, the bounded control signals confirm that the controller achieves a trade-off between performance and duty cycle limitations.

4.4 Stability Analysis of Closed-loop System

Based on the LMI feasibility conditions, there exists a common quadratic Lyapunov function $V(\xi) = \xi^T P \xi$, with $P = X^{-1} > 0$, such that the closed-loop system matrix $(\hat{A}_i + \hat{B}K)$ satisfies the Lyapunov quadratic stability for all vertices of the polytopic model. To further illustrate the robustness of the synthesized controller under internal resistance variations, an eigenvalue (λ) analysis of the closed-loop system is additionally performed. This analysis ensures that closed-loop stability is preserved across the entire polytopic domain and provides a comprehensive validation of the robustness of the proposed control synthesis.

The eigenvalues of the closed-loop state matrix are computed using (27) for each vertex at matrix $(\hat{A}_i + \hat{B}K)$ in (14) to verify that all system poles remain in the left-half complex plane. The closed-loop system is stable if all eigenvalues $\lambda < 0$.

$$det[\lambda I - (\hat{A}_i + \hat{B}K)] = 0; \text{for } i = 1, 2, \dots, 16 \qquad (27)$$

The analysis is conducted on the closed-loop system for all controller schemes. In the stabilization scheme, an eigenvalue analysis is performed for all vertices of the polytopic model to examine the closed-loop pole locations under disturbances $\tilde{w}(t)$ applied to the battery current $\tilde{y}_1(t)$ and the DC bus voltage $\tilde{y}_2(t)$. In the tracking scheme, the closed-loop eigenvalues are analyzed with respect to the reference-to-output dynamics, specifically from the battery current reference $\tilde{r}_1(t)$ to the battery current output $\tilde{y}_1(t)$ and from the DC bus voltage reference $\tilde{r}_2(t)$ to the DC bus voltage output $\tilde{y}_2(t)$.

Fig. 8(a) and Fig. 8(b) show the closed-loop eigenvalues analysis for the stabilization scheme across all vertices of the polytopic model. In this result, all closed-loop poles remain strictly in the left-half plane for every vertex, thereby confirming robust asymptotic stability under parameter variations and external disturbances. In the tracking scenarios Fig. 8(c) and Fig. 8(d), which examine the reference-to-output dynamics, the closed-loop poles are likewise confined to the left-half plane, ensuring stable reference tracking. It is worth noting that the analysis reveals the presence of right-half plane zeros, indicating a non-minimum phase behavior inherent to the power conversion dynamics. While these right-half plane zeros impose fundamental limitations on achievable transient performance, they do not compromise internal stability, as stability is solely determined by pole locations. The absence of pole migration into the right-half plane across all vertices demonstrates that the proposed controller guarantees robust closed-loop stability for both stabilization and tracking objectives over the entire polytopic domain.

The closed-loop eigenvalue distributions reported in Table 3 confirm the robust stability of the proposed controller across the entire polytopic domain and clearly reflect the effect of tuning the LMI performance parameter μ. For the stabilization scheme (Table 3), all eigenvalues remain strictly in the left-half plane for vertex 1, the nominal model, and vertex 16, with

Table 3
Eigenvalues of closed-loop system for stabilization, tracking, and tracking with stabilization schemes

Control schemes	λ	Vertex 1	Current sys	Vertex 16
Stabilization	1	-3.2138×10^6	-3.2138×10^6	-3.2138×10^6
	2	-9.8277×10^4	-9.8280×10^4	-2.5000×10^5
	3	-4.9993×10^4	-7.8113×10^4	-9.8277×10^4
	4	-2.7556×10^2	-3.9968×10^2	-9.8684×10^2
	5	-2.0029×10^2	-3.0094×10^2	-2.8591×10^2
	6	-0.1197×10^2	-0.1168×10^2	-0.1094×10^2
	7	-0.1519×10^2	-0.1479×10^2	-0.1455×10^2
Tracking	1	-1.1689×10^7	-1.1689×10^7	-1.1689×10^7
	2	-2.4626×10^5	-2.4626×10^5	-2.4625×10^5
	3	-4.9998×10^4	-7.8124×10^4	-2.5001×10^5
	4	-2.2555×10^2	-4.2800×10^2	-1.0013×10^3
	5	-1.1408×10^2	-1.3865×10^2	-1.4389×10^2
	6	-0.3439×10^2	-0.1076×10^2	-0.2831×10^2
	7	-0.1065×10^2	-0.3055×10^2	-0.1034×10^2
Tracking with stabilization	1	-4.0031×10^6	-4.0031×10^6	-4.0031×10^6
	2	-1.1002×10^5	-1.1002×10^5	-2.5000×10^5
	3	-4.9992×10^4	-7.8114×10^4	-1.1002×10^5
	4	-3.4399×10^2	$-385.87 + 49.38i$	-9.8113×10^2
	5	-2.0291×10^2	$-385.87 - 49.38i$	-3.5963×10^2
	6	-0.1324×10^2	-0.1290×10^2	-0.1209×10^2
	7	-0.1648×10^2	-0.1615×10^2	-0.1599×10^2

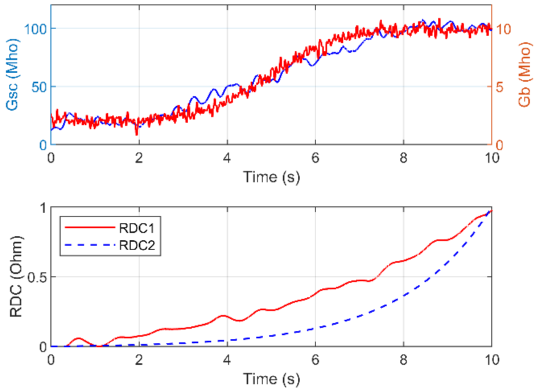

Fig. 9 Internal resistance variation for Batt-SC HPS system

dominant poles located at -3.2138×10^6, while the slowest modes are still sufficiently damped at approximately -10.34. A similar trend is observed for the tracking scheme, where the dominant eigenvalues shift further left, e.g., -1.1689×10^7, indicating faster convergence due to the inclusion of reference tracking dynamics. The majority of eigenvalues in both cases are real, which is a direct consequence of selecting a relatively small μ that enforces strong damping through the L2-gain constraint, favoring monotonic and non-oscillatory responses suitable for the Batt–SC HPS control system. In the combined tracking and stabilization scenario, all eigenvalues remain stable, with dominant poles at -4.0031×10^6 across all vertices, while a pair of complex-conjugate poles emerges in the intermediate modes ($-385.87 \pm 49.38i$ in the nominal case). This oscillatory behavior arises from the interaction between the integrator-based tracking dynamics and the stabilization loop when both objectives are enforced simultaneously, slightly relaxing the effective damping of certain modes. Nevertheless, the real parts of these complex poles remain on the order of -10^2, ensuring rapid decay of oscillations and preserving robust stability, thereby illustrating the trade-off introduced by μ between transient speed, overshoot, and robustness under parameter variations.

4.5 Simulation Result for Parameter Variation Profiles and Comparison with PID and LTI State-Feedback

In addition to being tested at its vertices in schemes 1, 2, and 3, the closed-loop system is also evaluated by involving parameter variations, as shown in Fig. 9. The purpose of this test is to examine the stability of the system against parameter variations, even though the controller is statically designed and guarantees stability only for the vertex systems. In addition, the controller performance is benchmarked against a PID controller whose parameters are tuned using MATLAB's auto-tuning and LMI-based state-feedback with an LTI model.

The internal resistance variation profiles are designed with different behaviors to mimic actual parameter changes. The conductance profiles of the Batt-SC system are shaped using a rising Gaussian function and a partial linear function, respectively, while the internal converter resistances are shaped

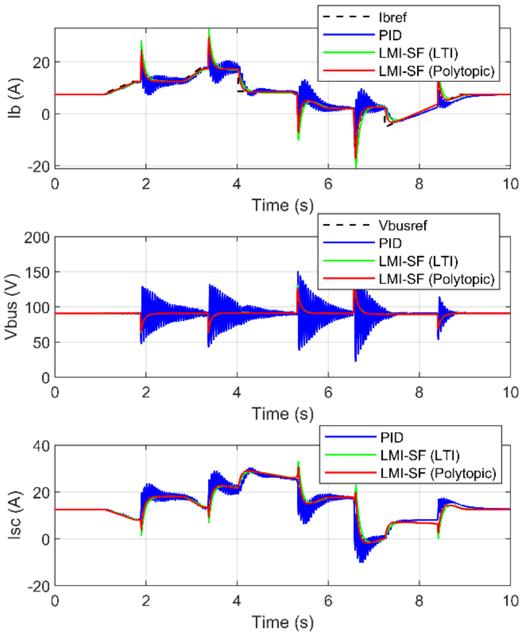

Fig. 10 Responses of battery current, DC bus voltage, and SC current under internal resistance variation

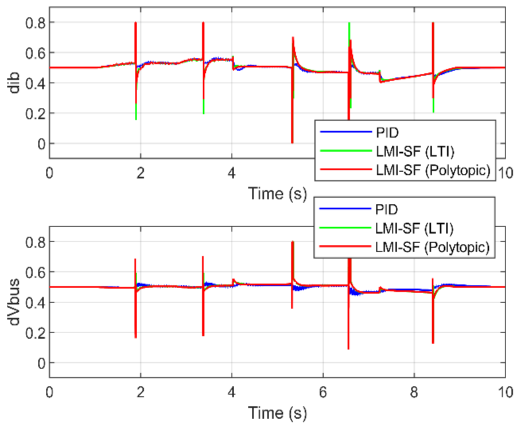

Fig. 11 Control signals under internal resistance variation

using rising exponential functions. These four parameter variations change within predetermined ranges. To resemble actual behavior, noise components of several frequencies are added. High-frequency noise is added to the G_b profile, medium-frequency noise to the G_{sc} profile, low-frequency noise to the R_{DC1} profile, and no noise is added to R_{DC2}. Nevertheless, these scenarios can still be considered idealized and could be further enhanced by incorporating more realistic parameter variations. For simplicity, this scenario is evaluated only for the last control scheme, as this scheme has the most complete LMI formulation, i.e., stability, L2-gain disturbance attenuation/tracking performance, and sector nonlinearity. The resulting output responses are shown in Fig. 10, while the control signals are depicted in Fig. 11.

As shown in Fig. 10, the PID controller exhibits pronounced oscillations and overshoot in all controlled variables, particularly during load transients and reference changes. In contrast, the proposed controller achieves significantly smoother responses with faster settling times and reduced overshoot. For the battery current, the proposed controller closely tracks the reference while effectively suppressing high-frequency oscillations, indicating improved current regulation and reduced stress on the battery. Similarly, the DC bus voltage under the proposed controller remains tightly regulated around its reference with minimal overshoot, whereas the PID controller produces large voltage ripples during transient events with a maximum overshoot 77.93%. Furthermore, the supercapacitor current response demonstrates that the proposed controller provides more coordinated power sharing between the battery and the supercapacitor, resulting in enhanced transient compensation and improved overall system stability. These results confirm the effectiveness of the proposed control strategy in improving dynamic performance and robustness compared to the PID controller. Nevertheless, the PID controller produces control signals with smaller amplitudes compared to the proposed controller, as shown in Fig. 11. This behavior is attributed to the fact that the PID controller is tuned to minimize error locally, whereas the LMI-based design explicitly incorporates robustness and stability constraints, leading to increased but more effective control effort.

Table 4 compares the RMSE performance of the proposed simultaneous LMI-based state-feedback (LMI-SF) controller with a conventional PID controller in terms of battery current and DC bus voltage regulation. The results clearly demonstrate the superior performance of the LMI-SF controller. Specifically, the RMSE of the battery current is reduced from 2.0890 A under PID control to 0.6101 A, corresponding to a reduction of approximately 70.8%. Similarly, the DC bus voltage RMSE decreases significantly from 13.1100 V to 1.9999 V, achieving an improvement of about 87.4%. When compared with the LMI-based state-feedback controller synthesized using a nominal LTI model, the proposed controller also achieves lower RMSE values for both the battery current and the DC bus voltage, albeit with smaller margins. Specifically, the RMSE is reduced by 0.3790 A or 38.31% for the battery current and by 0.0581 V or 2.82% for the DC bus voltage. These substantial reductions indicate that the proposed controller provides more accurate tracking and disturbance rejection. This improvement is attributed to the explicit incorporation of system dynamics and stability constraints within the LMI-based design framework, which enables systematic handling of multivariable coupling and operating uncertainties. In contrast, the PID controller, tuned heuristically, exhibits limited capability in regulating both battery current and DC bus voltage simultaneously under dynamic conditions.

Table 4
RMSE comparison with PID and LTI controllers

Controllers	Battery current (A)	DC bus voltage (V)
PID	2.0890	13.1100
LMI-SF (LTI)	0.9891	2.0580
LMI-SF (Polytopic)	0.6101	1.9999

4.6 Power and Energy Comparison

In addition to stability and dynamic performance evaluation, power and energy analysis are conducted to further examine the impact of the proposed controller on the power flow characteristics of the Batt–SC HPS. Although the proposed simultaneous LMI-based state-feedback controller is not explicitly designed for energy optimization, this analysis aims to verify whether the enhanced robustness against parameter

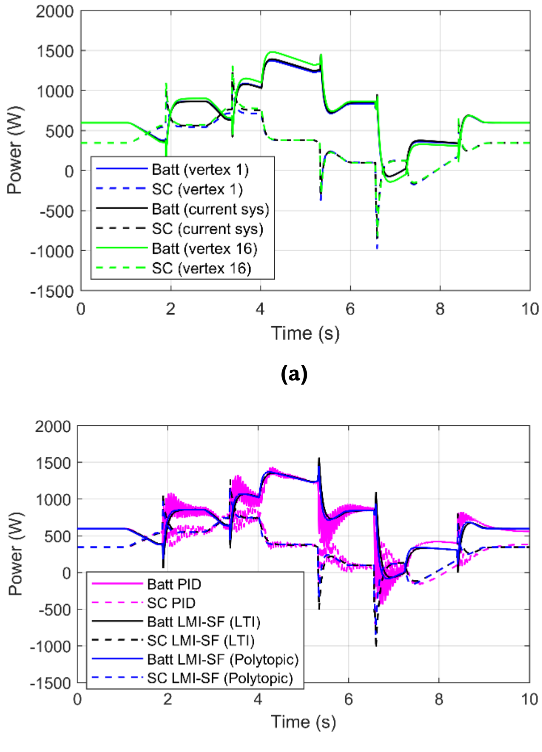

(b)

Fig. 12 Power consumption comparison: (a) at vertex 1, current sys, and vertex 16, (b) the proposed controller with PID and LTI controllers

Table 5
Energy comparison at the system vertex

Energy comparison based		Battery (Joule)	SC (Joule)	Total (Joule)
Vertex	1	3,299	6,966	10,265
	Current sys	3,385	6,999	10,384
	16	3,430	7,119	10,549
Controllers	PID	3,330	6,942	10,272
	LMI-SF (LTI)	3,333	6,916	10,249
	Polytopic	3,345	6,916	10,261

variations is achieved without imposing a significant energy penalty compared to conventional controllers. Power and energy consumption analyses are conducted under vertex conditions as well as under internal resistance variation profiles, with comparisons made against other control strategies.

As illustrated in Fig. 12(a), the overall power profiles of the battery and supercapacitor remain qualitatively similar across all vertices, indicating consistent closed-loop behavior under parameter variations. However, variations in instantaneous power levels are observed during transient events, particularly at vertex 16, which corresponds to a more extreme combination of system parameters. Despite these transient differences, the accumulated energy remains within a narrow range. Fig. 12(b) shows that all controllers exhibit comparable power profiles, while noticeable differences appear during transient conditions.

The total energy increases from vertex 1 to the nominal system and reaches vertex 16, corresponding to relative increases of 1.16% and 2.77%, respectively, as listed in Table 5. These results demonstrate that, although the proposed controller exhibits vertex-dependent power redistribution during transients, the resulting energy variation remains limited, confirming robust energy behavior across the entire polytopic variations domain. The energy calculation for different controllers is also performed by integrating the power profile over time. The calculation results are also presented in Table 5. The results indicate that all controllers yield very similar energy consumption levels. Compared to the PID controller, the total energy difference is 0.22% for the LMI-SF (LTI) controller and 0.11% for the proposed LMI-SF (polytopic) controller. Moreover, the difference between the two LMI-based controllers is only 0.12%, confirming that the variations are negligible. These results demonstrate that the proposed controller achieves enhanced robustness and constraint handling without introducing a meaningful increase in power consumption, which is beneficial for maintaining energy-efficient and reliable operation of Batt-SC HPS in EV applications.

5. Conclusion

This paper has presented the state-feedback control synthesis for a Batt-SC HPS system considering parameter variations and saturation constraints. Three LMI formulations have been numerically validated and simulated in the closed-loop system for the case of internal resistance variations. The results demonstrate that stability guarantees are achieved for all three schemes at vertex 1, vertex 16, and the selected system parameter. Furthermore, the synthesized controller still demonstrates satisfactory performance under the parameter variation profiles, even though this evaluation may appear exploratory, since the controller guarantees stability only at the vertices of the polytopic model. In addition to stability and dynamic performance, power and energy analysis indicate that, although the proposed controller may produce slightly higher transient power, the total energy exchanged by the system remains comparable to that of other controllers. Future work may extend the proposed controller synthesis by integrating the polytopic framework into the HLC strategy. In addition, hardware experiments can be conducted to further validate the effectiveness and practical applicability of the synthesized controller.

Acknowledgments

The authors would like to acknowledge the Indonesian Education Scholarship, the Center for Higher Education Funding and Assessment, and the Indonesian Endowment Fund for Education for their financial support of this work. The authors also thank the Laboratory for Control and Computer Systems, STEI ITB, for providing the facilities and resources that enabled this research.

Author Contributions: A. R. A: Conceptualization, methodology, formal analysis, writing—original draft, A. S. R: supervision, review and editing, resources, project administration, P. H. R: supervision, review and editing, validation, A. R: supervision, review and editing, project administration, validation. All authors have read and agreed to the published version of the manuscript.

Funding: This research was funded by the Indonesian Education Scholarship, Center for Higher Education Funding and Assessment, and Indonesian Endowment Fund for Education 2024 with Decree No. 00417/BPPT/BPI.06/9/2024.

Conflicts of Interest: The authors declare no conflict of interest.

References

Abdelhedi, R., Lahyani, A., Ammari, A. C., Sari, A., & Venet, P. (2018). Reinforcement learning-based power sharing between batteries and supercapacitors in electric vehicles. *Proceedings of the IEEE International Conference on Industrial Technology*, *2018-Febru*, 2072–2077. https://doi.org/10.1109/ICIT.2018.8352508

Abdelkader, A., Rabeh, A., Mohamed Ali, D., & Mohamed, J. (2018). Multi-objective genetic algorithm based sizing optimization of a stand-alone wind/PV power supply system with enhanced battery/supercapacitor hybrid energy storage. *Energy*, *163*, 351–363. https://doi.org/10.1016/j.energy.2018.08.135

Ahmad, W., Khan, L., Khan, Q., & Ullah, I. (2024). Advanced Sliding Mode Control Techniques Employed on Electric Hybrid Vehicle. *2024 IEEE Texas Power and Energy Conference, TPEC 2024*, 1–6. https://doi.org/10.1109/TPEC60005.2024.10472230

Aini, S. F., Tahtawi, A. R. Al, Yahya, S., & Ilman, S. M. (2023). Linear Quadratic Integrator Control Design for Battery-Supercapacitor Hybrid Energy Storage System. *2023 10th International Conference on Information Technology, Computer, and Electrical Engineering (ICITACEE)*, 236–241. https://doi.org/10.1109/ICITACEE58587.2023.10276761

Al Tahtawi, A. R., Rohman, A. S., Rusmin, P. H., & Rizqiawan, A. (2025a). Dynamic model and control strategies of battery-supercapacitor hybrid power sources for electric vehicles : a review. *International Journal of Power Electronics and Drive Systems*, *16*(2), 695–709. https://doi.org/10.11591/ijpeds.v16.i2.pp695-709

Al Tahtawi, A. R., Rohman, A. S., Rusmin, P. H., & Rizqiawan, A. (2025b). On the Robust Stability of Battery-Supercapacitor Hybrid Power Sources in Electric Vehicles. *2025 12th International Conference on Information Technology, Computer, and Electrical Engineering (ICITACEE)*, 1–6. https://doi.org/10.1109/ICITACEE66165.2025.11232969

Amin, Bambang, R. T., Rohman, A. S., Dronkers, C. J., Ortega, R., & Sasongko, A. (2014). Energy Management of Fuel Cell/Battery/Supercapacitor Hybrid Power Sources Using Model Predictive Control. *IEEE Transactions on Industrial Informatics*, *10*(4), 1992–2002. https://doi.org/10.1109/TII.2014.2333873

Apkarian, P., Gahinet, P., & Becker, G. (1995). Self-scheduled H∞ control of linear parameter-varying systems: a design example. *Automatica*, *31*(9), 1251–1261. https://doi.org/10.1016/0005-1098(95)00038-X

Bai, Z., Yan, Z., Wu, X., Xu, J., & Cao, B. (2019). H∞ control for battery/supercapacitor hybrid energy storage system used in electric vehicles. *International Journal of Automotive Technology*, *20*(6), 1287–1296. https://doi.org/10.1007/s12239-019-0120-x

Bourenane, H., Berkani, A., Negadi, K., Marignetti, F., & Hebri, K. (2023). Artificial Neural Networks Based Power Management for a Battery/Supercapacitor and Integrated Photovoltaic Hybrid Storage System for Electric Vehicles. *Journal Europeen Des Systemes Automatises*, *56*(1), 139–151. https://doi.org/10.18280/jesa.560118

Boyd, S., El Ghaoui, L., Feron, E., & Balakrishnan, V. (1994). Linear Matrix Inequalities in System and Control Theory. In *Society for Industrial and Applied Mathematics (SIAM)* (Vol. 15).

Dao, H. V, To, X. D., Truong, H. V. A., Do, T. C., & Ho, C. M. (2021). Optimization-based fuzzy energy management strategy for PEM fuel cell/battery/supercapacitor hybrid construction excavator. *International Journal of Precision Engineering and Manufacturing-Green Technology*, *8*, 1267–1285. https://doi.org/10.1007/s40684-020-00262-y

Golchoubian, P., & Azad, N. L. (2017). Stochastic nonlinear model predictive control of battery-supercapacitor hybrid energy storage systems in electric vehicles. *2017 American Control Conference*. https://doi.org/10.23919/ACC.2017.7963189

Huang, S., Zhu, X., Sarkar, S., & Zhao, Y. (2019). Challenges and opportunities for supercapacitors. *APL Materials*, *7*(10). https://doi.org/10.1063/1.5116146

IEA. (2025). *Global EV Outlook 2025*. https://www.iea.org/reports/global-ev-outlook-2025

Islam, M. M., Siffat, S. A., Ahmad, I., & Liaquat, M. (2021). Adaptive Nonlinear Control of Unified Model of Fuel Cell , Battery , Ultracapacitor and Induction Motor Based Hybrid Electric Vehicles. *IEEE Access*, *9*, 57486–57509. https://doi.org/10.1109/ACCESS.2021.3072478

Itani, K., Bernardinis, A. De, Khatir, Z., Jammal, A., Member, S., & Oueidat, M. (2016). Regenerative Braking Modeling , Control , and Simulation of a Hybrid Energy Storage System for an Electric Vehicle in Extreme Conditions. *IEEE Transactions on Transportation Electrification*, *2*(4), 465–479. https://doi.org/10.1109/TTE.2016.2608763

Jia, C., Cui, J., Qiao, W., & Qu, L. (2023). Real-Time Model Predictive Control for Battery-Supercapacitor Hybrid Energy Storage Systems Using Linear Parameter-Varying Models. *IEEE Journal of Emerging and Selected Topics in Power Electronics*, *11*(1), 251–263. https://doi.org/10.1109/JESTPE.2021.3130795

Jung, H., Wang, H., & Hu, T. (2014). Control design for robust tracking and smooth transition in power systems with battery/supercapacitor hybrid energy storage devices. *Journal of Power Sources*, *267*, 566–575. https://doi.org/10.1016/j.jpowsour.2014.05.061

Khan, M. A., Zeb, K., Sathishkumar, P., Ali, M. U., Uddin, W., Hussain, S., Ishfaq, M., Khan, I., Cho, H. G., & Kim, H. J. (2018). A novel supercapacitor/lithium-ion hybrid energy system with a fuzzy logic-controlled fast charging and intelligent energy management system. *Electronics (Switzerland)*, *7*(5), 1–19. https://doi.org/10.3390/electronics7050063

Larijani, M. R., Kia, S. H., Zolghadri, M., Hajjaji, A. El, & Taghavipour, A. (2024). Linear Parameter-Varying Model Predictive Control for Intelligent Energy Management in Battery/Supercapacitor Electric Vehicles. *IEEE Access*, *12*, 51026–51040. https://doi.org/10.1109/ACCESS.2024.3385861

Lemian, D., & Bode, F. (2022). Battery-Supercapacitor Energy Storage Systems for Electrical Vehicles: A Review. *Energies*, *15*(15). https://doi.org/10.3390/en15155683

Maghfiroh, H., Wahyunggoro, O., & Cahyadi, A. I. (2024). Optimal Sizing and Improved Low-Pass Filter Energy Management for Hybrid Energy Storage Electric Vehicles. *IEEE Access*, *12*, 180926–180938. https://doi.org/10.1109/ACCESS.2024.3509481

Mossadak, M. A., Chebak, A., Ouahabi, N., Rabhi, A., & Elmahjoub, A. A. (2024). A Novel Hybrid PI--Backstepping Cascade Controller for Battery--Supercapacitor Electric Vehicles Considering Various Driving Cycles Scenarios. *IET Power Electronics*, *17*(9), 1089–1105. https://doi.org/10.1049/pel2.12697

Mulder, E. F., Kothare, M. V., & Morari, M. (2015). Multivariable anti-windup controller synthesis using iterative linear matrix inequalities. *European Control Conference, ECC 1999 - Conference Proceedings*, *37*, 3531–3536. https://doi.org/10.23919/ecc.1999.7099877

Naseri, F., Farjah, E., & Ghanbari, T. (2017). An efficient regenerative braking system based on battery/supercapacitor for electric, hybrid, and plug-in hybrid electric vehicles with BLDC motor. *IEEE Transactions on Vehicular Technology*, *66*(5), 3724–3738. https://doi.org/10.1109/TVT.2016.2611655

Sadeq, T., & Wai, C. K. (2020). Linear Quadratic Regulator Control Scheme on Hybrid Energy Storage System. *2020 IEEE International Conference on Automatic Control and Intelligent Systems (I2CACIS)*, 219–223. https://doi.org/10.1109/I2CACIS49202.2020.9140093

Saw, L. H., Poon, H. M., Chong, W. T., Wang, C. T., Yew, M. C., Yew, M. K., & Ng, T. C. (2019). Numerical modeling of hybrid supercapacitor battery energy storage system for electric vehicles. *Energy Procedia*, *158*, 2750–2755. https://doi.org/10.1016/j.egypro.2019.02.033

Siffat, S. A., Ahmad, I., Ur Rahman, A., & Islam, Y. (2020). Robust integral backstepping control for unified model of hybrid electric vehicles. *IEEE Access*, *8*, 49038–49052. https://doi.org/10.1109/ACCESS.2020.2978258

Song, Z., Hou, J., Hofmann, H., Li, J., & Ouyang, M. (2017). Sliding-mode and Lyapunov function-based control for battery/supercapacitor hybrid energy storage system used in electric vehicles. *Energy*, *122*, 601–612. https://doi.org/10.1016/j.energy.2017.01.098

Song, Z., Li, J., Hou, J., Hofmann, H., Ouyang, M., & Du, J. (2018). The battery-supercapacitor hybrid energy storage system in electric vehicle applications: A case study. *Energy*, *154*, 433–441. https://doi.org/10.1016/j.energy.2018.04.148

Suthar, M., Manthati, U. B., Arunkumar, C. R., Srinivas, P., Alsaif, F., & Zaitsev, I. (2024). Enhancing Electric Vehicle Performance with a Hybrid PI-Sliding Mode Controller for Battery Supercapacitor Integration. *International Journal of Energy Research*, *2024*, 1–13. https://doi.org/10.1155/2024/1105301

Syahbana, D. F., & Trilaksono, B. R. (2019). MPC and Filtering-Based Energy Management in Fuel Cell/ Battery/ Supercapacitor Hybrid Source. *2019 International Conference on Electrical Engineering and Informatics (ICEEI)*, 122–127. https://doi.org/10.1109/ICEEI47359.2019.8988849

Udeogu, C. U., & Lim, W. (2022). Improved Deep Learning-Based Energy Management Strategy for Battery-Supercapacitor Hybrid Electric Vehicle With Adaptive Velocity Prediction. *IEEE Access*, *10*, 133789–133802. https://doi.org/10.1109/ACCESS.2022.3232062

Vukajlović, N., Milićević, D., Dumnić, B., & Popadić, B. (2020). Comparative Analysis of the Supercapacitor Influence on Lithium Battery Cycle Life in Electric Vehicle Energy Storage. *Journal of Energy Storage*, *31*, 101603. https://doi.org/10.1016/j.est.2020.101603

Xu, D., Liu, Q., Yan, W., & Yang, W. (2019). Adaptive Terminal Sliding Mode Control for Hybrid Energy Storage Systems of Fuel Cell, Battery and Supercapacitor. *IEEE Access*, *7*, 29295–29303. https://doi.org/10.1109/ACCESS.2019.2897015

Zand, M., Nasab, M. A., Hatami, A., Kargar, M., & Chamorro, H. R. (2020). Using Adaptive Fuzzy Logic for Intelligent Energy Management in Hybrid Vehicles. *2020 28th Iranian Conference on Electrical Engineering (ICEE)*, 1–7. https://doi.org/10.1109/ICEE50131.2020.9260941

Zhang, Q., Deng, W., & Li, G. (2017). Stochastic control of predictive power management for battery/supercapacitor hybrid energy storage systems of electric vehicles. *IEEE Transactions on Industrial Informatics*, *14*(7), 3023–3030. https://doi.org/10.1109/TII.2017.2766095

Zhang, X., Lu, Z., Yuan, X., Wang, Y., & Shen, X. (2021). L2-Gain Adaptive Robust Control for Hybrid Energy Storage System in Electric Vehicles. *IEEE Transactions on Power Electronics*, *36*(6), 7319–7332. https://doi.org/10.1109/TPEL.2020.3041653

Zhang, X., Wang, Y., Yuan, X., Shen, Y., & Lu, Z. (2023). Adaptive dynamic surface control with disturbance observers for battery/supercapacitor-based hybrid energy sources in electric vehicles. *IEEE Transactions on Transportation Electrification*, *9*(4), 5165–5181. https://doi.org/10.1109/TTE.2022.3194034

Zhao, Y., Qin, F., & Zhang, Z. (2025). Robust Tracking Control Design of Hybrid Battery-Supercapacitor Energy Storage System in Electric Vehicles. *IEEE Transactions on Transportation Electrification*, *11*(1), 3262–3276. https://doi.org/10.1109/TTE.2024.3436650

Zheng, S., Wang, K., & Xu, W. (2017). Fuzzy logic-based control strategy for a battery/supercapacitor hybrid energy storage system in electric vehicles. *2017 Chinese Automation Congress (CAC)*, 5598–5601. https://doi.org/10.1109/CAC.2017.8243780

Zhong, Q., Xie, C., Jin, S., Li, B., & Shi, K. (2021). New optimal control algorithms for battery-supercapacitor HESS based on Wirtinger-based integral inequality. *IEEE Access*, *9*, 17707–17716. https://doi.org/10.1109/ACCESS.2021.3053065